Geochemistry, Geophysics, Geosystems

Supporting Information for

Earthquake-swarms, slow-slip and fault-interactions at the western-end of the Hellenic Subduction System precede the M_w 6.9 Zakynthos Earthquake, Greece

Vasiliki Mouslopoulou[1,3*], Gian-Maria Bocchini[2], Simone Cesca[3], Vasso Saltogianni[3], Jonathan Bedford[3], Gesa Petersen[3], Michael Gianniou[4,5], Onno Oncken[3]

[1]National Observatory of Athens, Institute of Geodynamics, Athens, 11810, Greece (vasiliki.mouslopoulou@noa.gr)

[2]Ruhr University of Bochum, Institute of Geology, Mineralogy and Geophysics, Germany (Gian.Bocchini@rub.de)

[3]GFZ Helmholtz Centre Potsdam, German Research Centre for Geosciences, Telegrafenberg 14473 Potsdam, Germany (cesca@gfz-potsdam.de; salto@gfz-potsdam.de; jbed@gfz-potsdam.de; gesap@gfz-potsdam.de; oncken@gfz-potsdam.de)

[4] Hellenic Cadastre, Athens, 15562, Greece (mgianniu@ktimatologio.gr)

[5]University of West Attica, Athens, 12243, Greece (mgianniou@uniwa.gr)

Contents of this file

Additional Supporting Information (Files uploaded separately)

Introduction

The following text (Text S1-S6) and data (Supplementary Figs S1-S17, Supplementary Tables S1-S6 and Movies S1-S3) present details on the calculation of various seismic parameters (b-value, magnitude of completeness, etc.), calculation of moment tensor solutions, analysis and modeling of GPS data and analysis of fault kinematics, complementing those included in the article: 'Earthquake-swarms, slow-slip and fault-interactions at the western-end of the Hellenic subduction system precede the M_w 6.9 Zakynthos Earthquake, Greece'.

In detail:

Text S1. Calculation of b-value, M_c and conversion of M_L to M_W

B-values are here calculated for the time-period of between Jan 31st 2013 and October 31st 2019 (Fig. 2d and Fig. S1c). Although there are earthquake data for the time-period prior to 2013, here we have decided to restrict our b-value analysis to the post 2013 time-period for the following reasons: a) Prior to January 31st 2011 all reported magnitudes are duration magnitudes (M_d) and not local magnitudes (M_L). As a result, the magnitudes of completeness are significantly larger (M_c>=3) prior to Feb. 1st 2011 than in the considered time span (average of about Mc=2.0±0.1) preventing, thus, any meaningful comparisons; and b) For the time period between February 1st, 2011 and December 31st, 2012 the magnitude of completeness (M_c) fluctuates significantly (see Fig. S1a), preventing the robust statistical calculation of b-values and their comparison with the subsequent time-intervals.

The magnitude of completeness (M_c) (Fig. 2b and Supplementary Figure S1) is calculated from the 'goodness-of-fit' test (Wiemer and Wyss, 2000), as the mean value over 1000 bootstrap runs using M_L published by the National Observatory of Athens (NOA). The b values reported in Fig. 2d are calculated as the mean value of 1000 bootstrap runs using the maximum-likelihood method (Aki, 1965; Utsu, 1965) and M_c constrained by the Goodness-of-Fit Test (Wiemer and Wyss, 2000). The events have been grouped in subsets of 500 earthquakes (with half-overlapping windows; starting from the mainshock time and going backwards in time) and the b-value for each subset is calculated (Fig. 2d and Fig. S1). The b-value for aftershocks is calculated for subsets of 1000 events. The greater number of events used for calculating b-values in the aftershock sequence obtains results which are thought to be less susceptible to possible changes in the number of events in the revised aftershock catalogue (the catalogue, as of February 2020, is still under revision). Nevertheless, the impact of such revision is minimal as the main analysis of this work concerns the period prior to the main Zakynthos Earthquake.

The seismic moment (Fig. 2c and Supplementary Table S1) is estimated by using the Hanks and Kanamori (1979) equation after converting M_L to M_w. The conversion from M_L to M_w was achieved by comparing the M_w obtained for a set of 102 events during moment tensor inversion (see Text S3) and the M_L adopted from NOA ($M_w = 0.975 * M_L + 0.323$).

Text S2. Earthquake relocation

Our preferred earthquake location software is the NLLoc (Lomax et al., 2000, 2009) that uses a non-linear location algorithm which is thought to provide more reliable solutions and hypocentre error estimates in case of ill-conditioned locations such as those encountered within the ZES. To reduce location errors and enhance the quality of the hypocentral solutions, we used only those phases from 30 stations located along the western coast of Peloponnese and the islands of Zakynthos and Kefalonia (22 HUSN seismographs and 8 temporary stations installed in western Peloponnese immediately after the mainshock; Fig. 1). The inclusion of additional seismic stations from central Peloponnese and/or northern Greece would have challenged the validity of our velocity model without reducing the azimuthal gap, because the crustal thickness between the mainshock region and central Peloponnese varies considerably (Pearce et al., 2012). Indeed, the average azimuthal gap for the analysed seismicity when all available HUSN stations are used is 212° (e.g. NOA solutions) while it is 216° when only the stations proximal to the ZES are analysed (Fig. 1; this study). We performed two runs in NLLoc to obtain the most accurate hypocentral solutions. The second run was performed to include travel-time residuals obtained from the first run. The inclusion of these residuals aims to correct for deviations from the 1-D velocity model at each station and improve the final solutions.

For the relocation we used a constant Vp/Vs ratio of 1.80 in accordance with other seismological studies in the area (Kassaras et al., 2016; Haddad et al., 2020). The earthquake catalogue and P and S phase picks herein were downloaded from the NOA website (http://bbnet.gein.noa.gr/HL/); last accessed in May 2019 for the period before the mainshock and November 2019 for the aftershocks**.** Furthermore, as of February 2019 the National Observatory of Athens has slightly changed the pick class qualities and associated errors for the standard routine earthquake analysis (Table S2). All relocated earthquakes are presented in the Supplementary Table S3.

Text S3. Regional moment tensor inversion, classification and decomposition

Regional moment tensor inversion has been performed for the mainshock and more than 100 earthquakes in the mainshock focal region following two full waveform-based approaches, using the Kiwi tools (Cesca et al., 2010, 2013) and Grond (Heimann et al. 2018) software. Both approaches are based on the fit of 3-components full waveforms and, in case of the first approach, the fitting of amplitude spectra. For this analysis we used regional broadband data from stations pertaining to the following networks: GE (GEOFON, 1993), IU (Albuquerque Seismological Laboratory (ASL)/USGS, 1988), II (Scripps Institution of Oceanography, 1986), G (IPGP and EOST, 1982) , MN (MedNet Project Partner Institutions, 1990), IV (INGV Seismological Data Centre, 2006), HT (Aristotle University of Thessaloniki, 1981), HL (National Observatory of Athens, 1997), HP (University of Patras, 2000), HA (University of Athens, 2008), AC (Institute of Geosciences, Energy, Water and Environment, 2002), 4A (INGV, 2009), X5 (Sokos, 2015). Data and metadata have been downloaded using the FDSN web services of Orfeus, INGV, NOA, IRIS and Geofon. Seismic data are restituted, integrated to displacement, demeaned, detrended and rotated to a radial-transversal-vertical coordinate system. Data quality have been manually assessed, and a number of traces have been removed, either because containing saturated waveforms, data gaps, large noise and/or overlap with seismic signals of other events. For each earthquake, we defined a range of epicentral distances and a frequency band for the inversion, based on the catalog magnitude. For the first approach using the Kiwi tools, the general choice was as follows: The epicentral range of distances have been fixed to 150-500 km, 75-400 km, 50-300 km and 30-300 km for events with magnitude above Ml 6, Ml 5-6, Ml 4-5, and below Ml 4, respectively. Similarly, the following four frequency bandpass filters have been used for the four ranges of magnitudes, respectively: 0.010-0.040 Hz, 0.025-0.050 Hz, 0.035-0.070 Hz and 0.040-0.080 Hz. For the second, independent approach using Grond, epicentral distances of 80-400 km and a frequency band of 0.02-0.07 Hz were considered. For both approaches these parameters have been slightly modified for few events, especially during the first hours of the sequence when signals of different earthquakes overlap, in order to improve the fit.

For the moment tensor inversions based on the Kiwi tools (Cesca et al., 2010), we use a pure double couple (DC) constraint for all events. Inversions are performed in two following steps, first fitting 3-component full waveform amplitude spectra to resolve the scalar moment, centroid depth, strike, dip and rake, but not the focal mechanism polarity (Cesca et al., 2010) and later in the time domain, to resolve the focal mechanism polarity and horizontal shifts of the centroid location. An example of the inversion results after these two inversion steps is shown in Fig. S3. We also tested the inversion using a full moment tensor configuration (Cesca et al., 2013), but judged that the non-DC terms are not robustly resolved for many earthquakes, due to the limited

azimuthal coverage and the weak magnitude of the target earthquakes. Therefore, in this work, a full MT solution is only discussed for the mainshock, where we obtain 72% DC, 18% CLVD and 10% isotropic component. The presence of a significant non-DC component and the ENE-WSW orientation and negative sign of the CLVD major axis are in agreement with reference solutions by Global CMT and Sokos et al. (2020). The second MT inversion using Grond (Heimann et al., 2018), is in this study based on the inversion of displacement traces only. An important advantage of Grond is that the moment tensor optimization is performed simultaneously simulating many station configurations using a bootstrap approach: analysing the ensemble of best solutions for different station configurations allows estimating source parameter uncertainties. Comparison of results and estimated uncertainties for selected parameters are illustrated in Fig. S4.

We processed 124 earthquakes, all those occurring in the time period 1.1.2014-31.5.2019 with local magnitude equal or larger than 4.0 and within latitudes 36.8°-38.0° and longitudes 19.5-21.6° according to our relocated catalog. Good quality moment tensor solutions have been obtained for a subset of 102 earthquakes, down to a moment magnitude Mw 3.9 (Table S4). The selection of best solutions was done upon the quality of the misfit after the two inversion steps.

Focal mechanisms of the 102 solutions are classified using a clustering algorithm (Cesca, 2020), using clustering parameters Nmin=2 and eps=0.16 (equivalent to 19.2° Kagan angle). We identify 8 clusters, representing ~77% of the focal mechanisms (Fig. S5). Clusters are characterized either by strike-slip mechanisms or by thrust and normal faulting mechanisms with oblique components. Two clusters located in the vicinity of the mainshock epicenter show trench parallel thrust faulting (red focal mechanisms in Fig. 5) and oblique (strike-slip to normal) mechanism (seagreen mechanisms in Fig. 5). These two types of mechanisms are observed for many early aftershocks and could thus map the geometry of faults activated during the mainshock, as found for previous complex earthquakes (e.g. Cesca et al., 2017). They also resemble the mechanisms proposed by Sokos et al. (2020) for two subfaults contributing to the Zakynthos earthquake rupture. Supposing that the two faults were active during the mainshock, their combined contribution could resemble the full MT solution of the mainshock and its non-DC component. A similar result has been shown for the 2017 Kaikoura earthquake, New Zealand (Cesca et al., 2017). Figure 6 in the main article shows how a combination of ~53% and ~47% oblique faulting can qualitatively reproduce the mainshock MT and its double couple.

Text S4. Depth estimation using seismic array at teleseismic distances

Hypocentral locations for offshore seismicity may suffer, in absence of dedicated amphibious seismic deployments, from the asymmetry of the land stations distribution and the large azimuthal gap. This problem can affect to a certain extent the analysis of the Zakynthos sequence, given the lack of local stations West of Zakynthos Island. Typically, the source parameter which is mostly affected is the source depth, which can have large uncertainties. Furthermore, there may be trade-offs among the resolved origin time, epicentral locations and depth. Here, we supplement the hypocentral relocation based on local onshore data, with an independent analysis at large distances using seismic arrays. This method has been used for the depth estimation of crustal seismicity in previous studies (e.g., Negi et al., 2017, Grigoli et al., 2018).

We stack seismic waveforms recorded at the seismic stations composing the GERES array, to construct a seismic beam, where the similar waveforms produced by a far distance earthquake (e.g. at Zakynthos) sum up constructively, in contrast to the uncorrelated seismic noise. As a result, we can obtain beams with a high signal-to-noise ratio for events of magnitude larger than Mw 4.5. We can then compare the observed beam with synthetic beams computed for the known moment tensor solution and variable source depths.

The following Figs. S6-S7 show two examples of comparison of observed and synthetic array velocity beams at the GERES array, Germany. The best depth is chosen upon a visual assessment of the fit, mostly aiming to reproduce the time delay of the pP arrival with respect to the first P onset. The pP phase travels from the earthquake focus to the surface (or the seafloor) and backward, later following a common path with the P phase. Thus the path difference among P and pP rays is the one traveled by the pP ray above the source. The pP-P delay measures the time needed for a P phase to travel two times above the hypocenter: the larger is the time delay, the larger the hypocentral depth. The absolute hypocentral depth can be directly inferred from this time delay, known the crustal velocity structure at the focal region.

In this work, we have obtained acceptable fits, and thus independent depth estimates (Supplementary Table S5), for 20 out of 24 tested events.

Text S5. GPS data, analysis and modeling

GPS data

As there are institutional/governmental restrictions associated with some of the raw geodetic data used in this study, we obtained the ITRF08 daily coordinates of 5 stations (TRIP, RLSO, PYRG, PYL1 and PAT0) available at the NEVADA Geodetic Laboratory (http://geodesy.unr.edu/magnet.php; Blewitt et al., 2018) and of 5 stations (063A, 003A, 028A, 030A, 029A) that belong to the HEPOS network of the Hellenic Cadastre. In both cases Precise Point Positioning (PPP) solutions were obtained. The NEVADA GPS coordinates have been processed using the GIPSY OASIS II (Jet Propulsion Laboratory, JPL) software while the HEPOS coordinates using the Canadian Spatial Reference System (CSRS) PPP software version 2.26.0. The discrepancies between the two solutions are of sub-mm level and are incorporated in the calculated velocity uncertainties (illustrated in Figure 7 in the main article and Movies S2 and S3 of the Supporting Information).

Stations ZAK2 and STRF on Zakynthos and Strofades islands, respectively, were not analyzed due to limited data (duration of timeseries <3yrs). Geodetic records of more than 3 years are required for reliable estimation of the noise level and other velocity characteristics in the GPS signal.

Optimum model solution derived from GRATSID:

Our optimum model solution (Fig. 2e) arises from a combination of the following two models: (i) pre-seismic model that derives by decomposing the pre-seismic signal only and (ii) post-seismic model that derives by decomposing the full-timeseries (1-1-2014 till 31-05-2019). This combined model was selected as the preferred solution because the 2018 transient signal was masked (Fig. S10) when we modelled the entire sequence (model ii) due to over-fitting of the large M6.9 offset on some of the stations (i.e., at station 028A these displacements reach ~40 mm and ~54 mm along the East and North component, respectively).

Forward modeling:

To better explore the origin and spatial distribution of these two transients we performed forward modelling and, assuming a homogeneous elastic half-space and using the analytical equations of Okada (1985), predicted surface displacements by assigning slip on the plate-interface (Fig. S12). The long wavelength of the GPS deformation pattern (Figure 7) suggests that aseismic slip has occurred beneath western/central Peloponnese in both SSEs of 2014 and 2018. In addition, maximum displacements are observed on Zakynthos Island, thus, implying slip at depth between mainland and the Island of Zakynthos. After testing for various displacement scenarios, we derived the best uniform-slip model for average slip of 5 mm on the plate-interface (Fig. S12c) and total geodetic moment release of 3.20×10^{25} dyne*cm (that corresponds to a Mw ~6.3 earthquake; Table S1) for each SSE, in good agreement with other transient signals globally (Supplementary Fig. S13) (i.e. Peng and Gomberg, 2010), a fact that reinforces the tectonic origin of these transients. Some discrepancies observed in the north of the study area (Fig. S12), likely reflect additional distributed slip on the plate-interface or/and upper-plate faults there. Thus, the estimated average slip of 5 mm on the plate-interface should be considered as the minimum slip required for reproducing the surface deformation observed in the study area**.**

Characteristics of the 2014 transient (network acceleration – SSE)
Transient duration: 24/9/2014-20/3/2015: 178 days
SSE duration: 29/11/2014-20/3/2015: 112 days = 112 * 24 * 3600= 9.6x10^6 s
Minimum moment released: 3.20x10^18 Nm

Characteristics of the 2018 transient (network acceleration – SSE – network acceleration)
Transient duration: 14/5/2018-25/10/2018: 164 days
SSE duration: 10/7/2018-30/9/2018: 107 days = 83 * 24 * 3600= 7.2x10^6 s
Minimum moment released: 3.20x10^18 Nm

Text S6. Strain budget within the ZES

The relative African-Eurasian plate-motion at the western-end of the HSS is ~26 mm/yr (Pérouse et al., 2017). A question that arises is what percentage of the plate-motion is accommodated by each process operating at the western-end of the HSS. To answer this question we have quantified the contribution of each component of deformation (seismic and aseismic) for the period that precedes the M_w 6.9 event (Supplementary Table S6). To calculate cumulative seismic moment along the orthogonal to the plate-motion transect C-C', we first converted local magnitudes (M_L) to moment magnitude (M_w) using an empirical relationship derived in this study ($M_w = 0.975 * M_L + 0.323$) and then calculated the seismic moment (M_0) using the the relation between M_0 and M_w (M_0= 10^(1.5*M_w+16.1); Hanks and Kanamori, 1979). We used calculated M_w for earthquakes for which we obtained focal mechanism solutions. The average slip (D) has been estimated using the equation M_0 = GDA (Aki, 1966), where the shear modulus (G) has been assumed equal to 30 GPa (standard value for the crust), M_0 has been calculated as described above along the 20 km wide transect C-C' (Fig. S16), while the fault area (A) has been estimated according to geometry of the subducting slab (see Fig. S16).

Total geodetic moment release, as obtained from the modeled aseismic events of 2014 and 2018 (Figure S12), is estimated at 6.40×10^{25} dyne*cm (Table S1). The seismic (1.3 mm/yr; Table S6) and geodetic (2.1 mm/yr; Table S6) slip rates accommodated in the study area due to earthquake and slow-slip events, respectively, are estimated over the observational period (4.8 years).

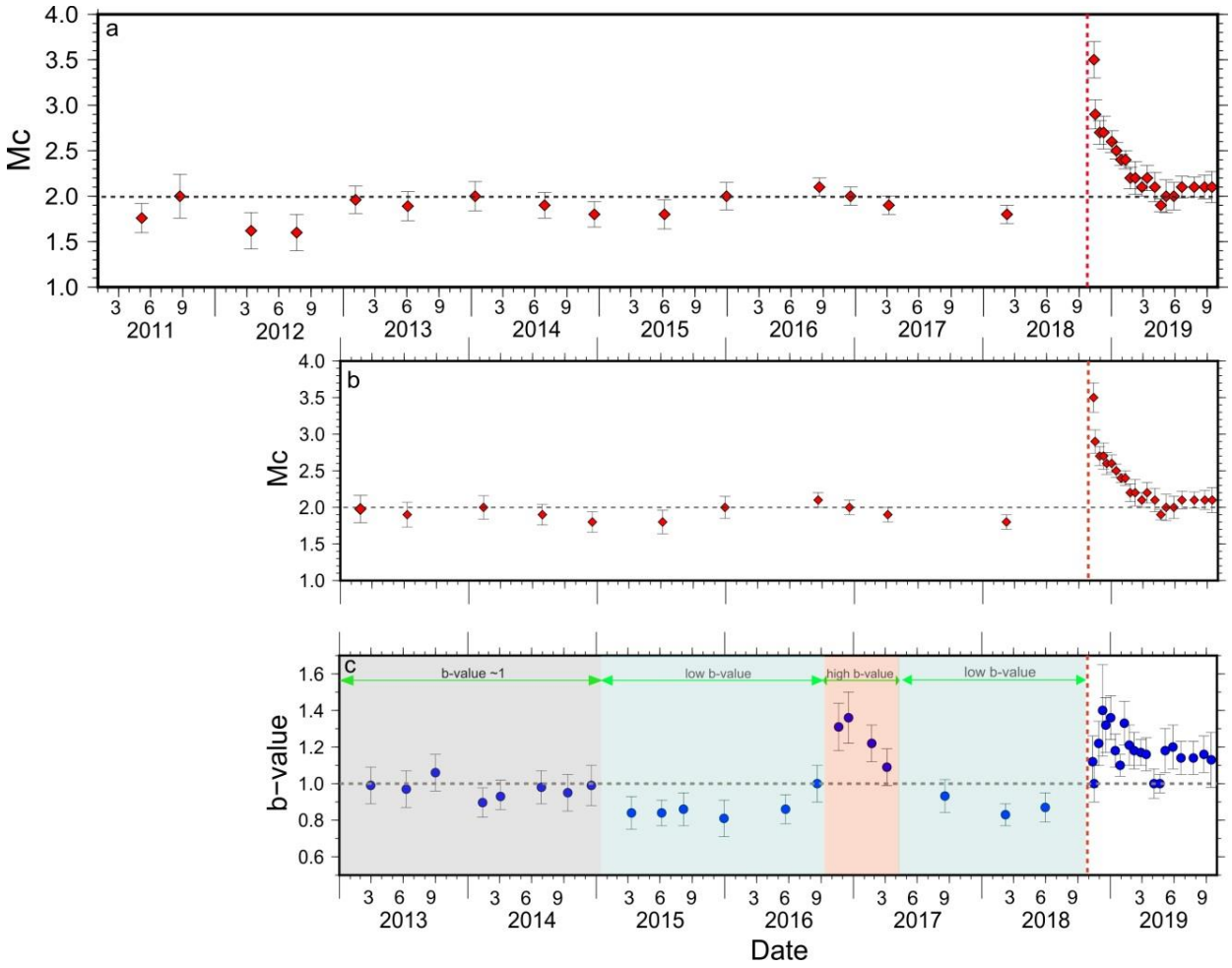

Figure S1. Graphs illustrating the evolution of the magnitude of completeness (a & b) and the b-values (c) in the study area for time periods from 1st January, 2011 to 31st October, 2019. Red dashed line indicates the timing of the M6.9 Zakynthos earthquake on October 25th, 2018. Note the fluctuating Mc values in 2012.

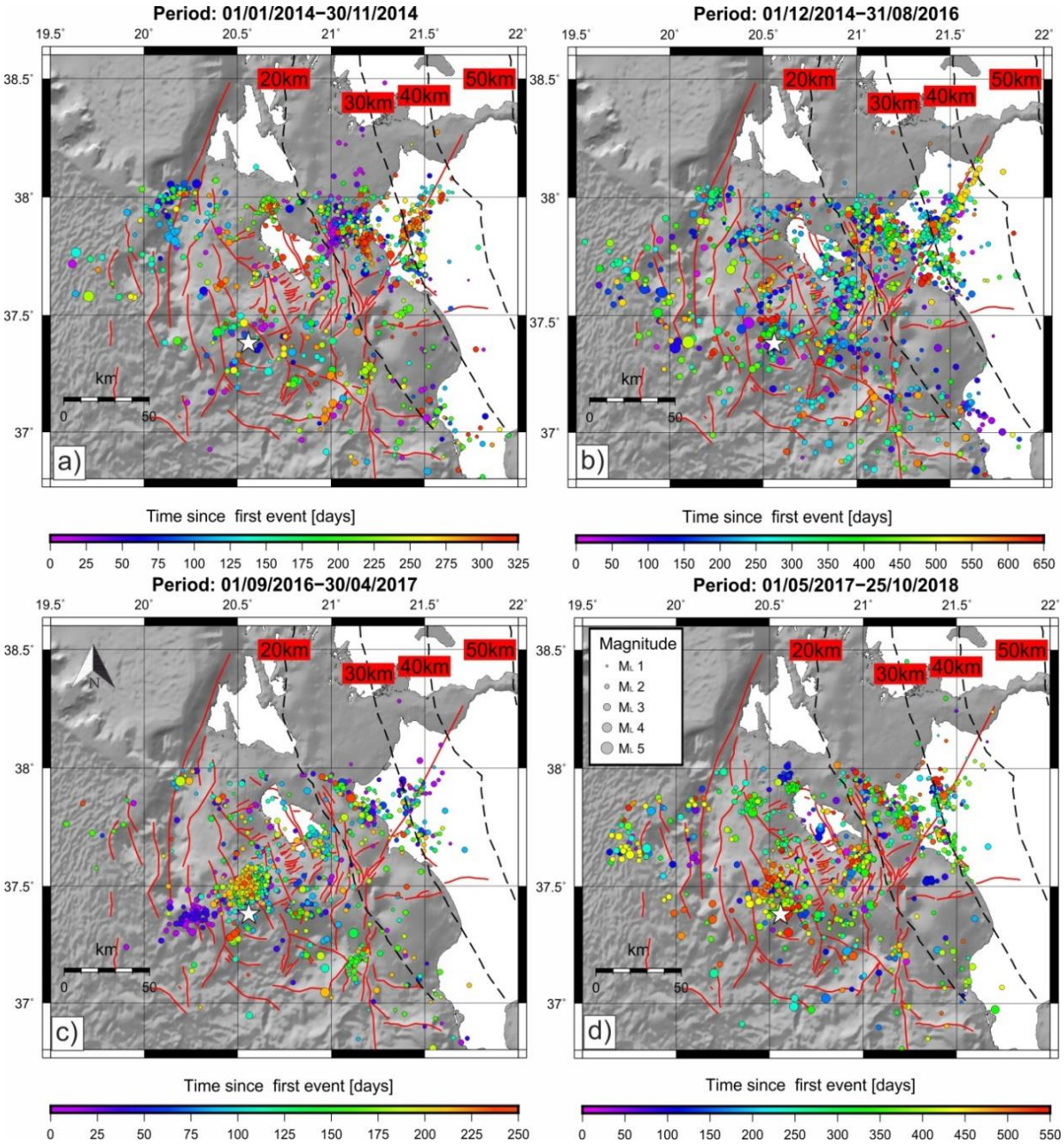

Figure S2. Map-view of the relocated foreshock ZES over four distinct time-intervals. Earthquake activity in each panel is colour-coded according to time (see legend). Seismic events have horizontal and vertical locations errors ≤25 km and RMS ≤1.5 sec. Black dashed lines in map-view and cross-section indicate the top of the plate-interface (from Halpaap et al., 2019) while white star indicates the M_w 6.9 epicentre. Bathymetry derives from https://www.gmrt.org/

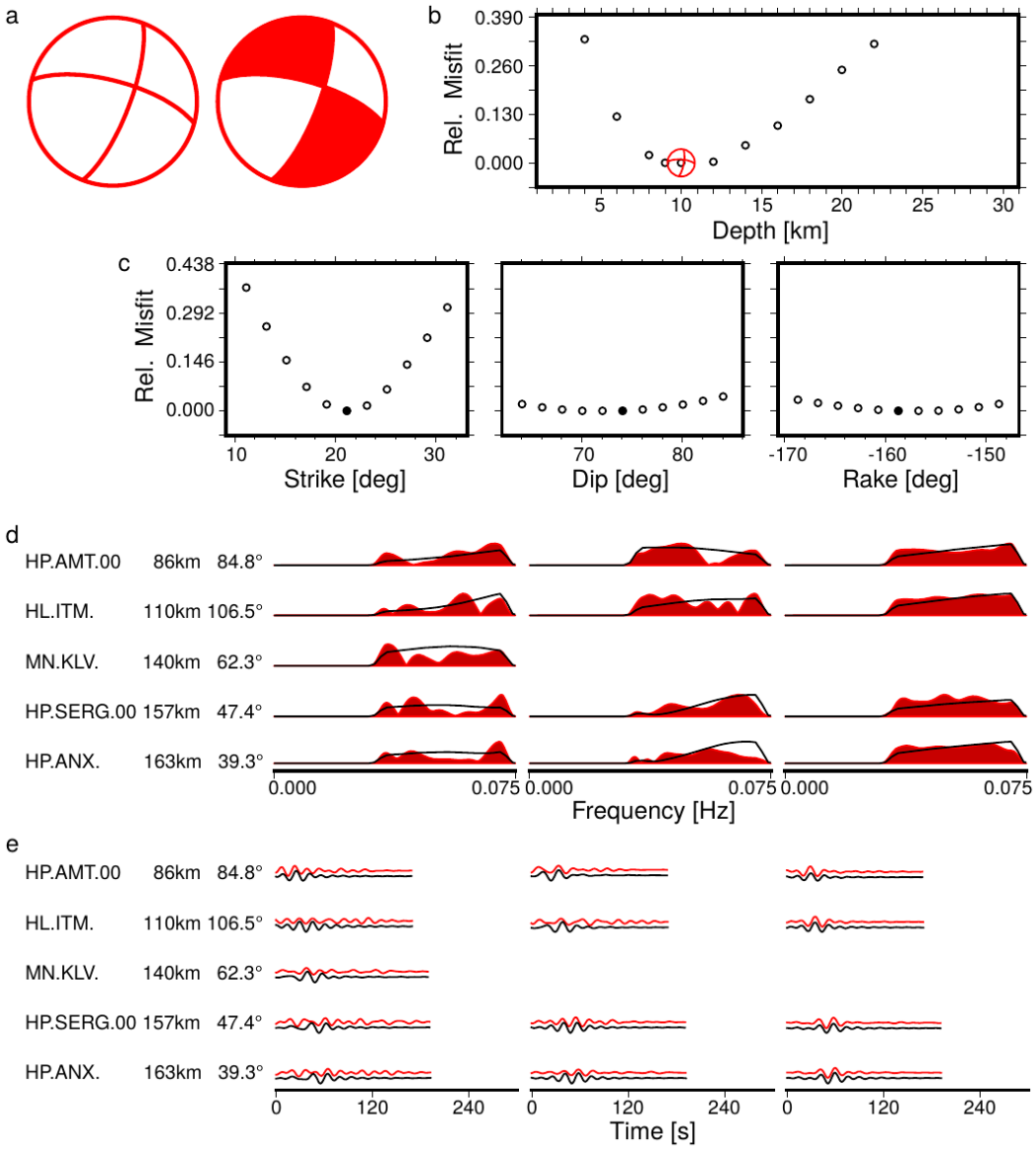

Figure S3. Example of moment tensor inversion result for the Zakynthos aftershock on 26.10.2018 at 12:11:17 UT: a, DC focal sphere after amplitude spectra inversion (white quadrants) and time domain inversion (red-white quadrants); b, relative misfit changes by perturbation of the source depth (the focal sphere denote the best solution); c, relative misfit changes by perturbation of strike, dip and rake (a solid circle denotes the best solution in each plot); d, comparison of observed (red) and synthetic (black) amplitude spectra along the vertical (left), radial (center) and transversal (right) components for selected stations (station names, epicentral distance and station azimuth are reported); e, comparison of observed (red) and synthetic (black) waveforms along the vertical (left), radial (center) and transversal (right) components for selected stations (station names, epicentral distance and station azimuth are reported).

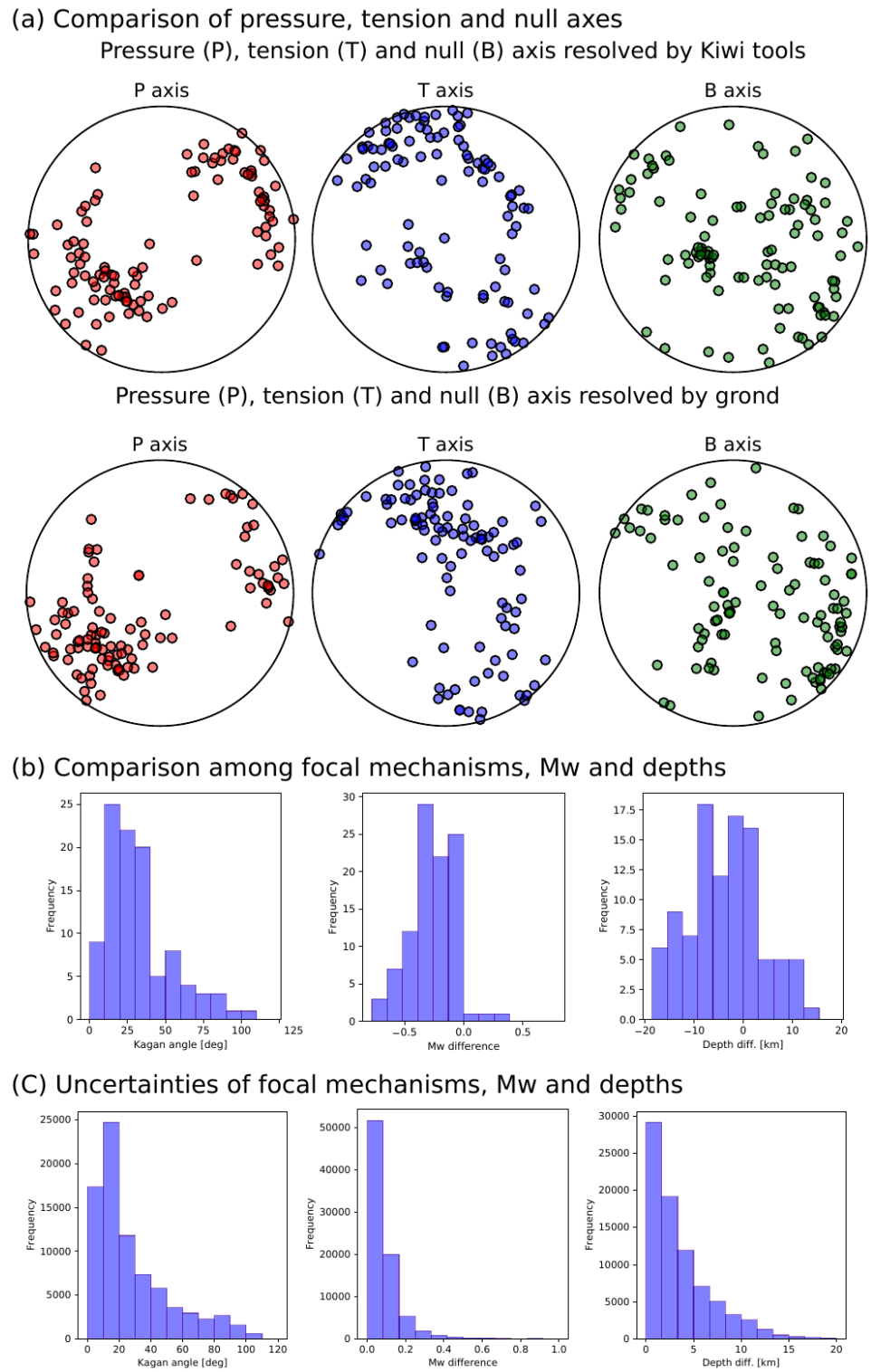

Figure S4. Comparison of solutions obtained for the same earthquakes with the Kiwi tools (Cesca et al. 2010, 2013) and Grond (Heimann et al. 2018) software, showing (a) the comparison of resolved pressure, tension, and null axes, (b) histograms with deviations among mechanisms (Kagan angle), moment magnitudes and depth estimates (values estimated by Kiwi tools minus those by Grond) and (c) histograms with uncertainties (focal mechanism orientations, moment magnitudes and depths) estimated by Grond though bootstrap: for each event, the inversion in Grond was run in parallel in 500 bootstrap chains with varying weightings of the fitting targets (station-component-phases combinations) as well as in one ‚global' chain in which weightings

only compensate station-event distances; uncertainties of our moment tensor solutions are assessed by comparing the best solution of each event to the ten best solutions of the 100 best performing bootstrap chains and the global chain; this approach assures meaningful statistics since we consider more than 1000 bootstrap solutions.

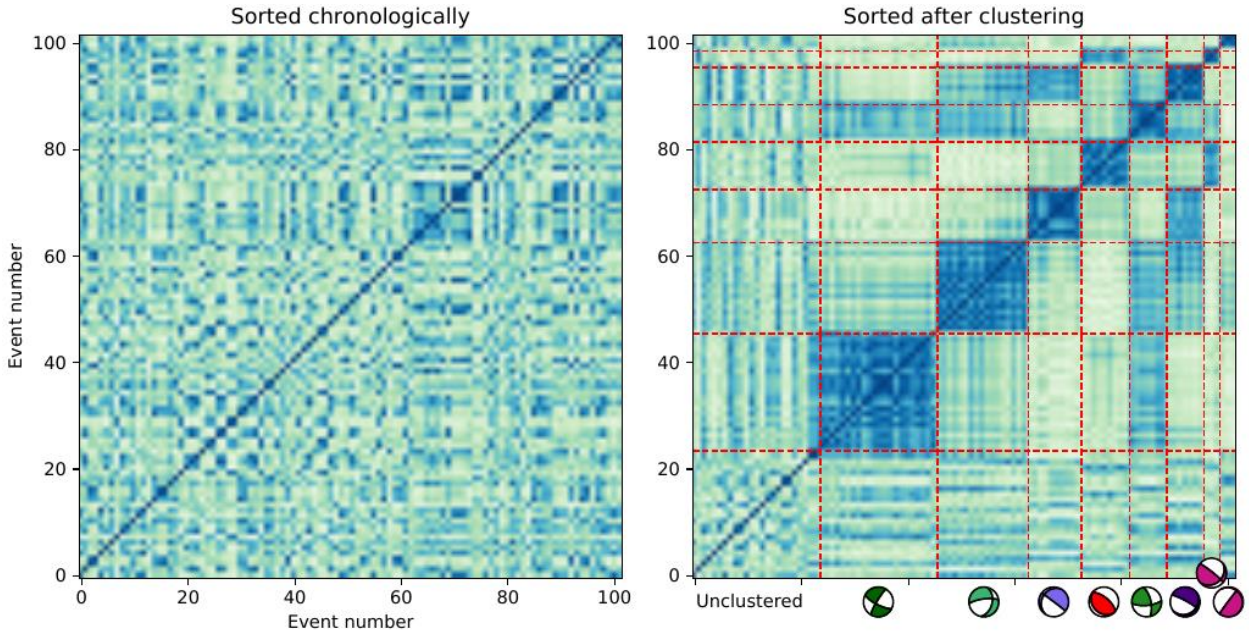

Figure S5. Results of the moment tensor clustering using seiscloud (Cesca 2020), showing similarity matrices for events sorted chronologically (left) and after clustering (right), where 8 clusters are identified (red dashed lines denote the edges of the clusters, focal mechanisms are representative (median) focal mechanisms for each clusters (colors as in Fig. 5); ~23% of the focal mechanisms remain unclustered.

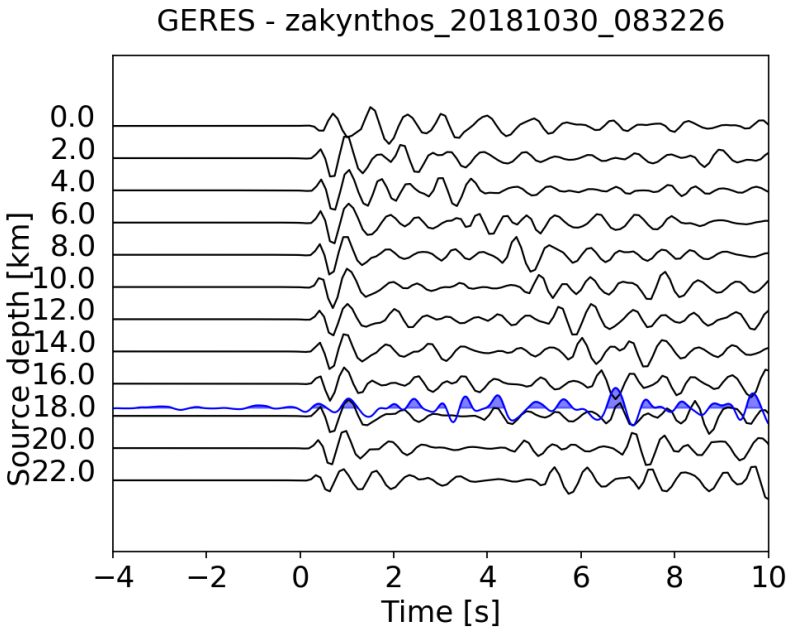

Figure S6. Comparison of the observed array beam at the GERES array, Germany, (blue) and synthetic beams for different depths (black lines), for an earthquake of the Zakynthos sequence occurring on 2018-10-30 at 08:32:26 UT. The best depth (here 17.5 km) is chosen upon a visual assessment of the waveforms fit. In particular, we aim to model the time delay of the pP arrival (here at ~ 6.5 s) with respect to the first P phase (0.0 s). Beams (here velocity waveforms) are bandpass filtered in the frequency range 0.7-2.0 Hz and normalized.

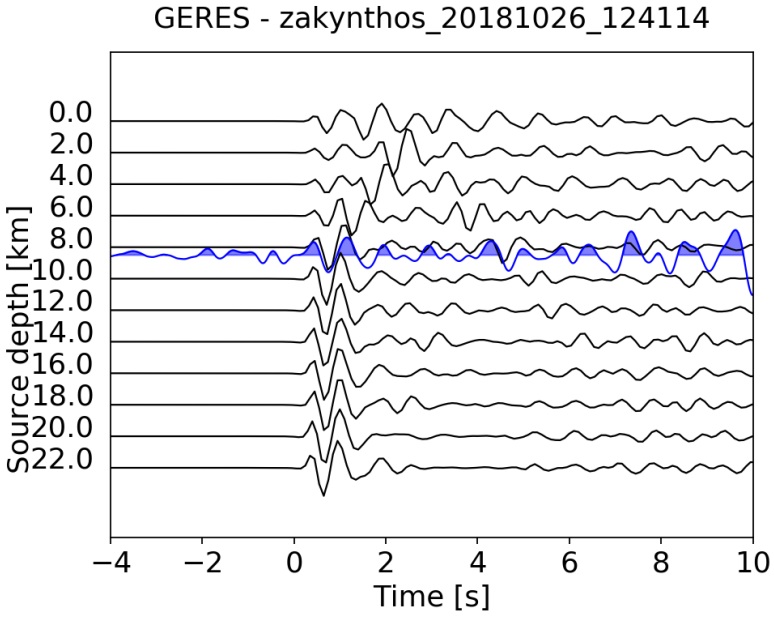

Figure S7. A second example (earthquake on 2018-10-26 12:41:14 UT) of comparison among observed and synthetic beams at the GERES array.

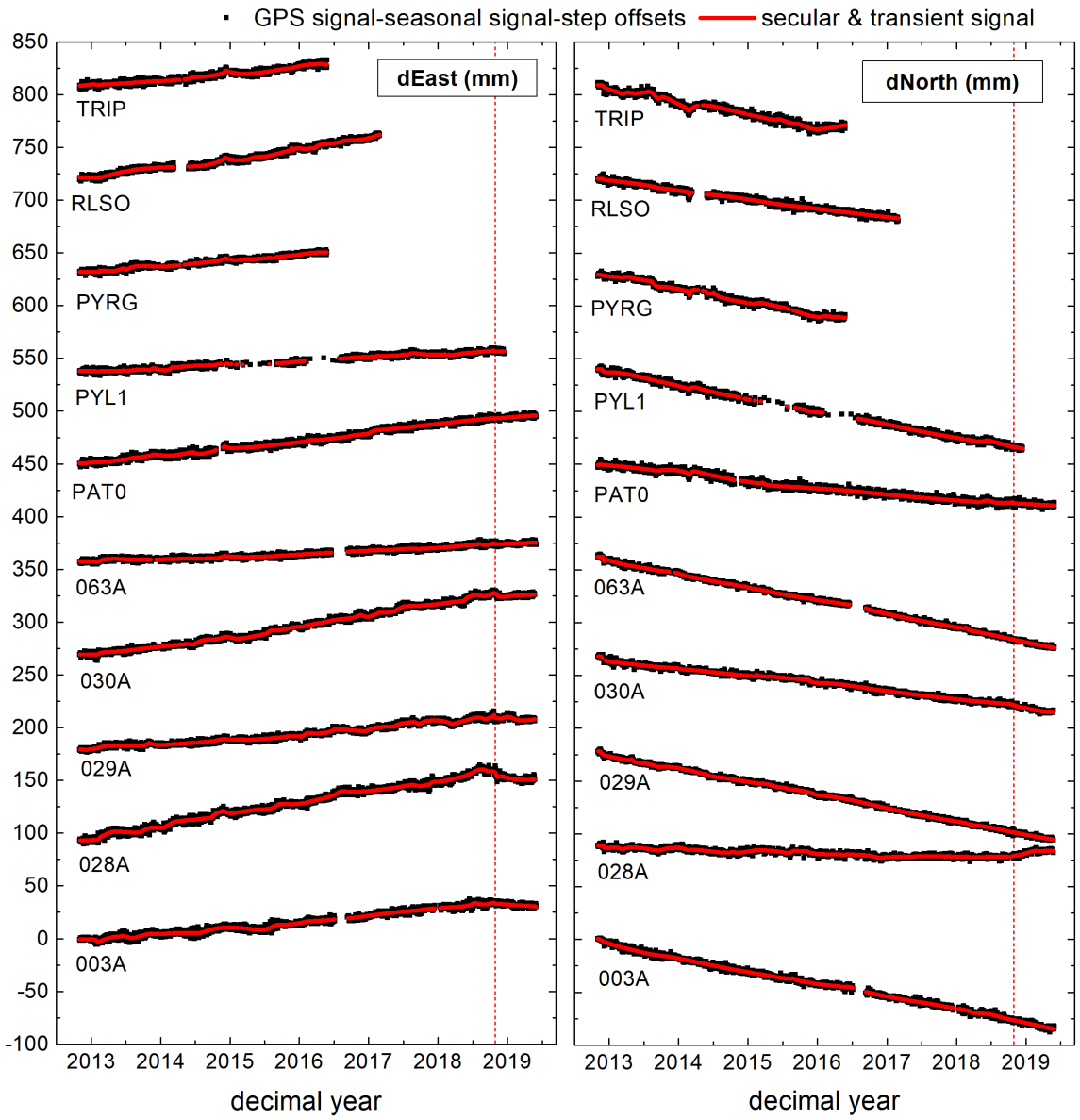

Figure S8. Timeseries of daily GPS coordinates analysed in this study along the East and North components. Filtered GPS signal, after subtracting the modeled seasonal and step-related signal, is indicated by black dots, while the decomposed transient GPS signal is indicated by the red line. Vertical red-dashed lines indicate the timing of the main-shock (October 25th, 2018).

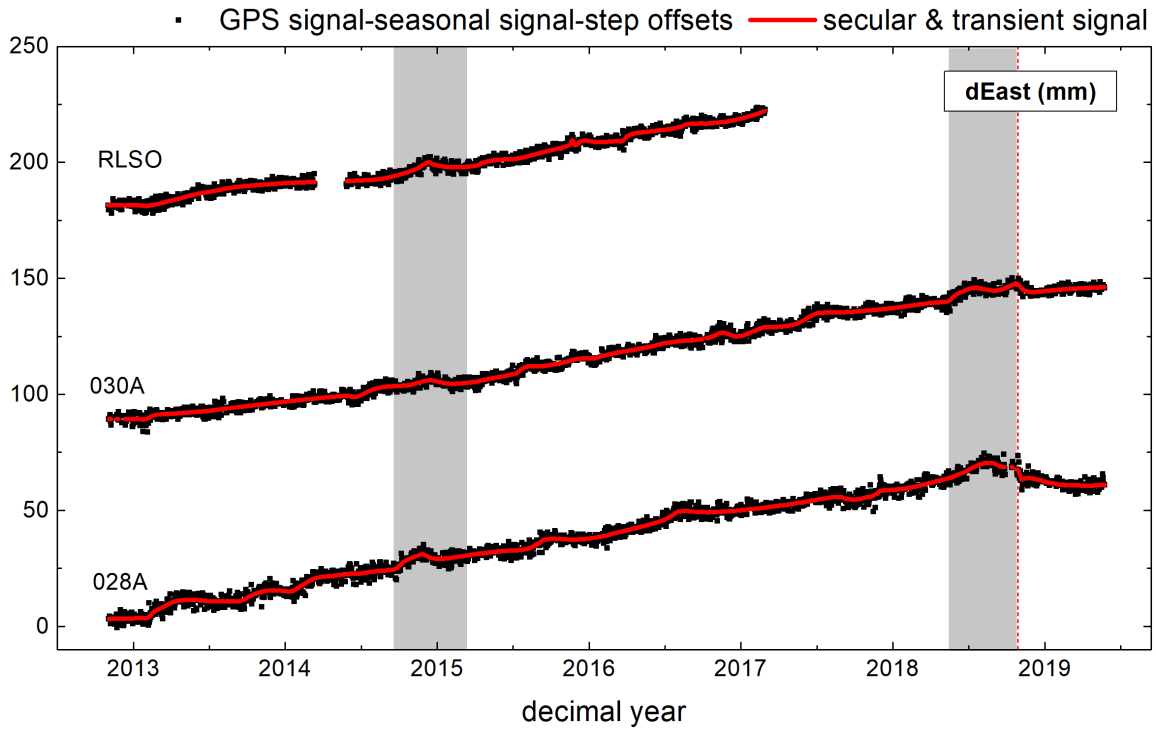

Figure S9. Similar to Figure S8, but for three selected GPS stations. Note the modelled 'wobbles' (Bedford et al. 2020) during the transient signals of 2014 and 2018.

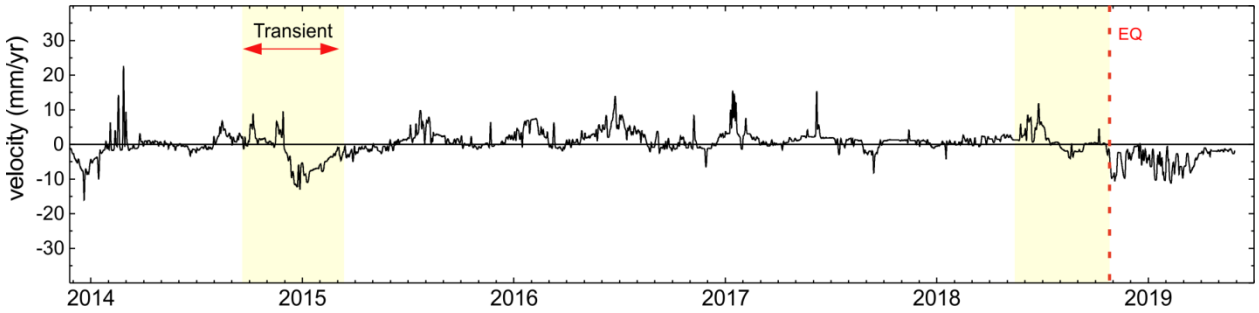

Figure S10. Evolution of the averaged GPS network velocity along the East component during the ZES, as derived from analysis of the entire pre and post-seismic GPS signal (model ii). The transient signal is clearly evident in late 2014, however, the 2018 transient signal before the mainshock (dashed red line), which is visible in Figure 2e, here is masked by the over-fitting of the seismic offset.

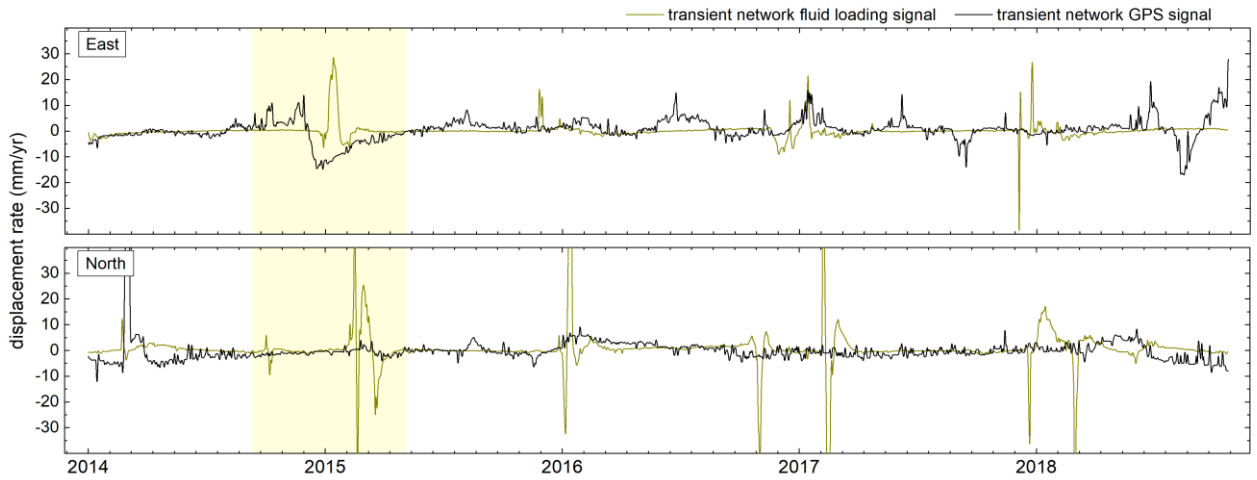

Figure S11. Modeled GPS transient signal (black line) and fluid loading (green line) signal averaged along the entire network along the East and North component. Shaded areas denote the major detected GPS transient signals.

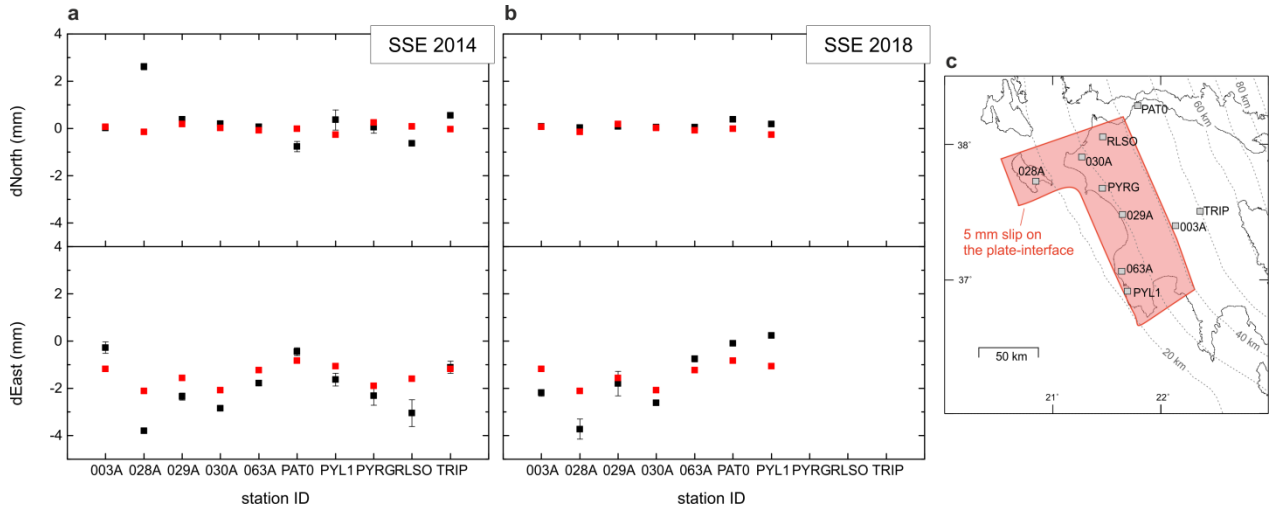

Figure S12. Results of the forward model. Predicted surface displacements (red dots) are compared with the observed GPS displacements (black dots) for the 2014 SSE (a) and the 2018 SSE (b), when slip of 5mm is assigned between the 20-40 km isodepths of the plate-interface and locally between the Zakynthos Island and Peloponnese.

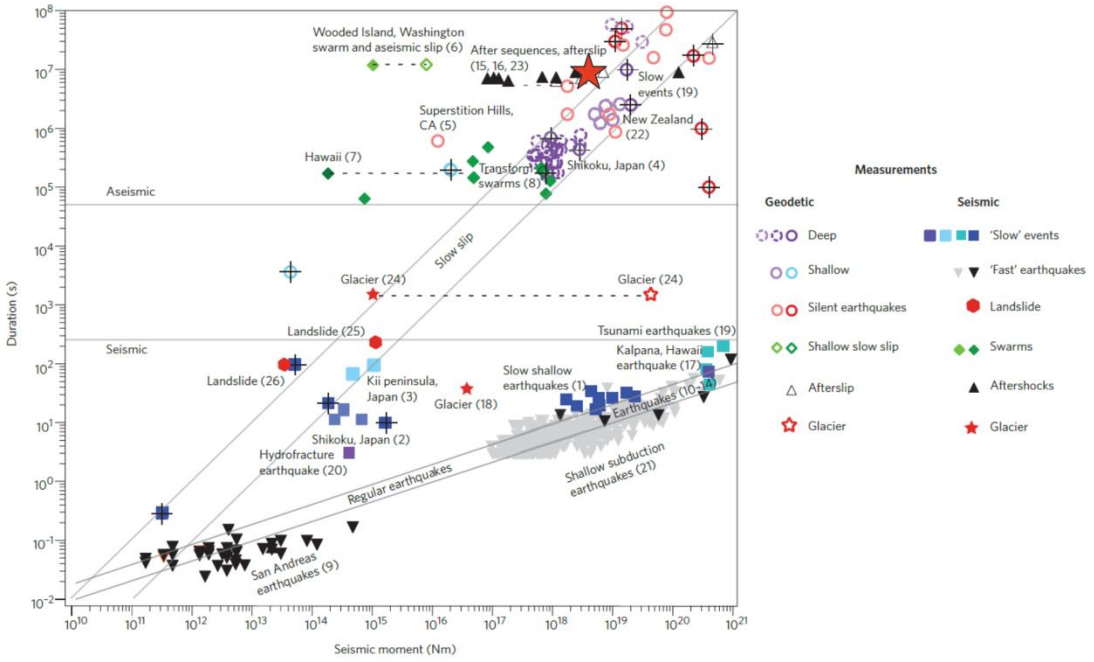

Figure S13. Graph showing the seismic moment versus source duration for a variety of fault-slip observations. Large red star indicates the 2014 and 2018 SSEs in the Hellenic margin. Figure modified from Peng & Gomberg (2010).

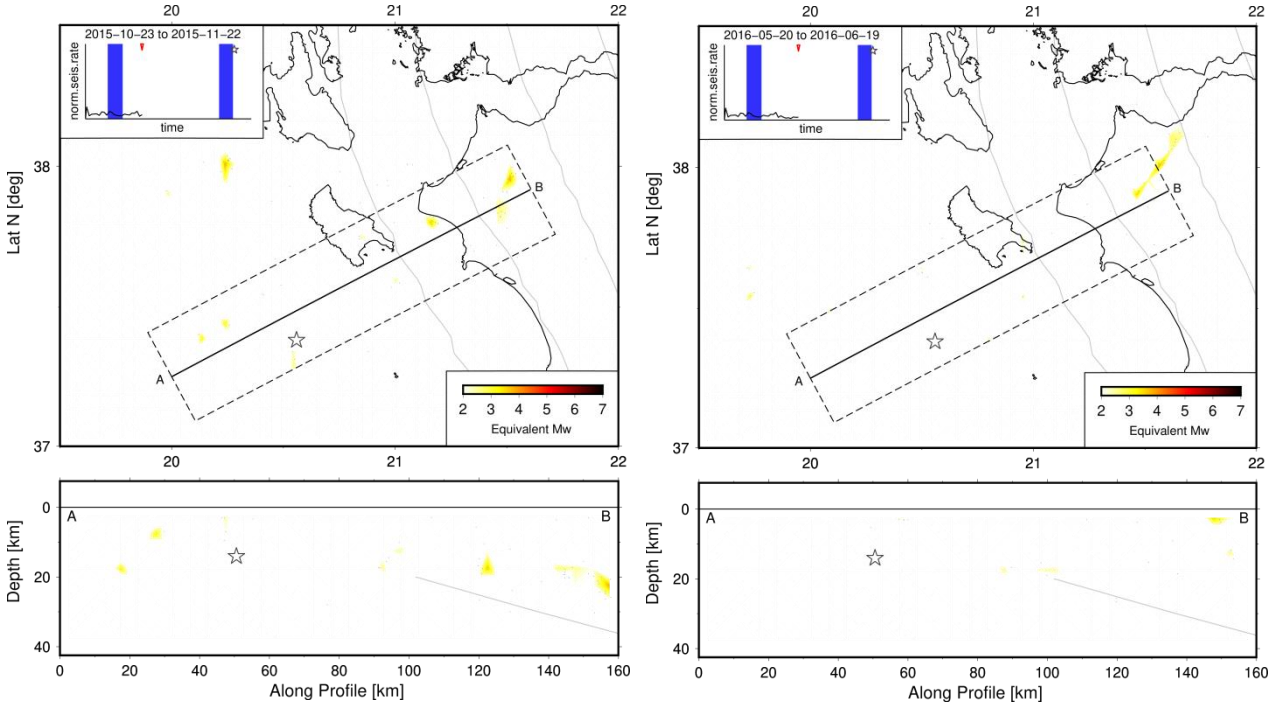

Figure S14. Snapshots of Movie S1 illustrating the seismicity recorded to delineate the Movri Fault from June to November 2015 and from May to August 2016. White star represents the epicentre of the October 25th, 2018 Mw 6.9 Zakynthos Earthquake.

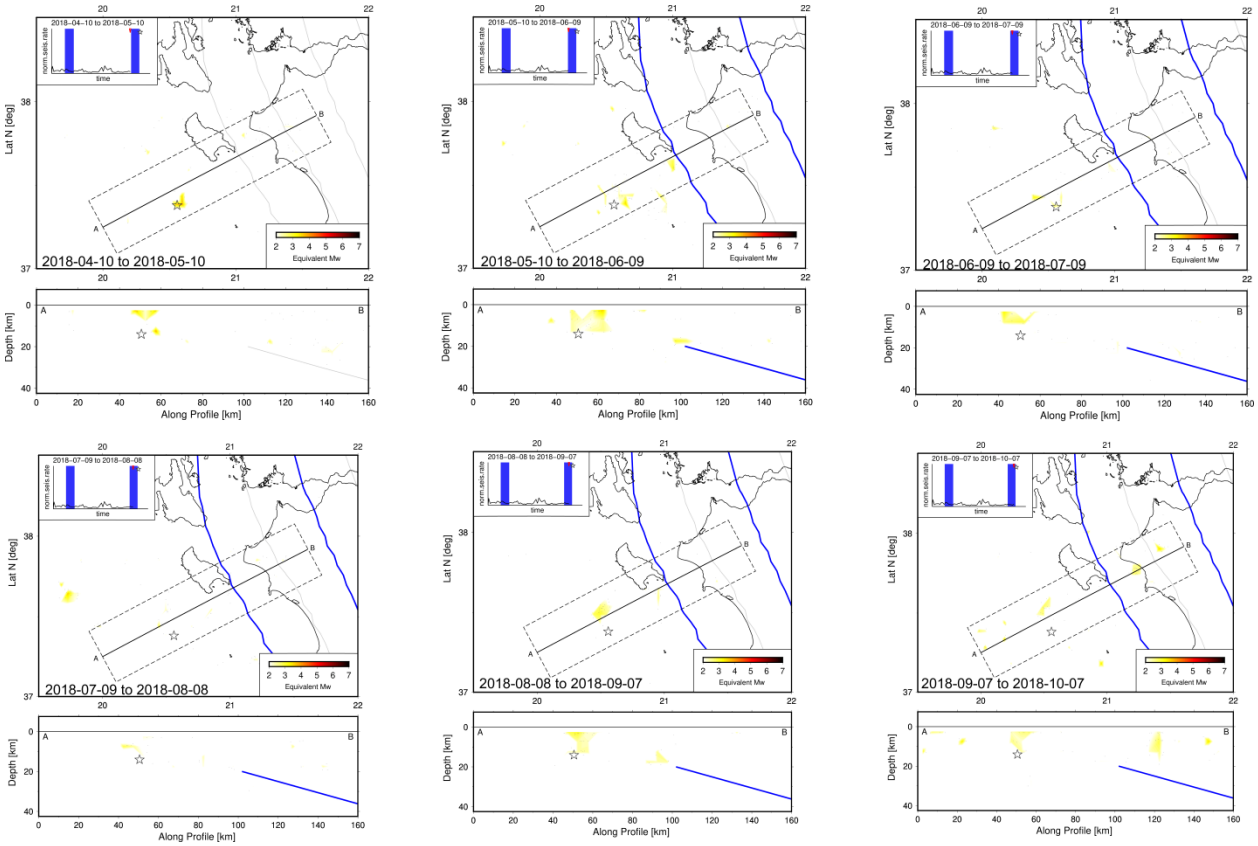

Figure S15. Snapshots of Movie S1 showing that clusters of shallow (<10 km) earthquakes occur within the epicentral area of the main Zakynthos event during the onset (May 2018) and throughout the 2nd transient. White star represents the epicentre of the October 25th, 2018 Mw 6.9 Zakynthos Earthquake.

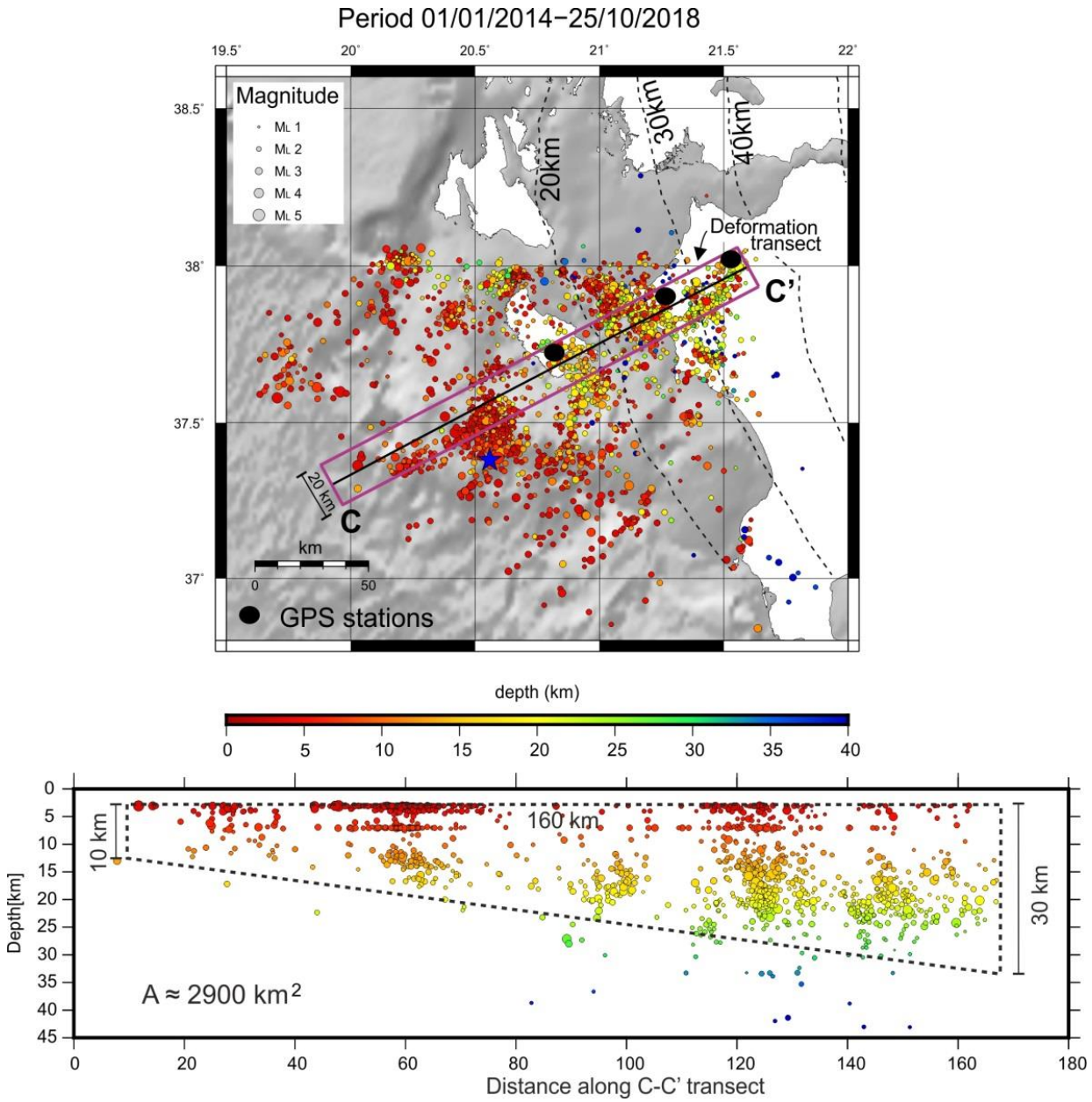

Figure S16. Transect over which the cumulative seismic (derived from earthquakes) moment release has been calculated. See text for details.

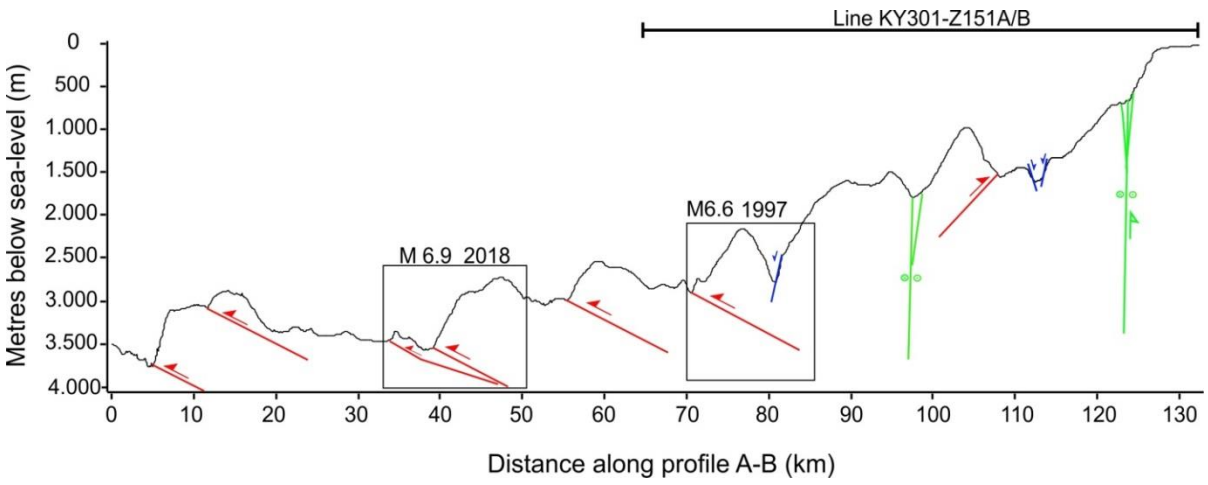

Figure S17. Bathymetric profile along the transect A-B (for locality see Fig. 1 in the main article) highlighting the control of active upper-plate faulting in the bathymetry. Faults are partly constrained by the interpretation of the seismic-reflection line KY301-Z151A/B presented in Fig. 4 and are colour coded according to Figs 1, 3, 4 and 7. The two thrust faults which are thought to have ruptured during the 1997 and 2018 M>6 earthquakes, are indicated. Vertical exaggeration x 10.

Table S1. Seismic moment released during the foreshock, aftershock and the entire ZES. Last column shows the % of the relative Eurasian-African plate-motion accommodated by each process.

Table S1	Seismic Moment (dyne-cm)	M_w	% of plate-motion
Foreshock sequence (Jan 1st, 2014 till Oct 25th 2018)	4.95×10^{24}	5.76	5%
Aftershock sequence excluding main event (Oct 25th, 2018 till May 31st 2019)	2.60×10^{25}	6.24	75%
Swarm-like activity (Sept. 2016 till Apr. 2017)	3.02×10^{23}	4.95	4.5%
Entire ZES (Jan. 1st, 2014 till May 31st 2019)	3.13×10^{26}	6.96	-
Slow Slip event 2014	3.24×10^{25} (min)	6.3	8%
Slow Slip event 2018	3.20×10^{25} (min)	6.3	

Table S2. Pick quality classes, and associated errors in seconds, during the ZES. Data are from the National Observatory of Athens (https://doi.org/10.7914/SN/HL).

Before February 2019		Since February 2019	
Pick quality class	Error (sec)	Pick quality class	Error (sec)
0	0.05	0	Unset
1	0.1	1	0.05
2	0.2	2	0.1
3	0.4	3	0.2
-	-	4	0.4

Table S3. Table presenting the attributes of all relocated earthquakes in the ZES (see uploaded .csv file).

Table S4: The moment tensor solutions that have been obtained for 102 ZES earthquakes (see uploaded .csv file).

Table S5. Hypocentral depths estimated for same Mw 4.5+ earthquakes of the Zakynthos sequence, estimated upon array beam modeling.

Date	**Time**	**Depth [km]**
2015-01-02	06:16:29	6.5
2015-12-12	08:34:47	6.5
2018-10-21	23:44:55	9.0
2018-10-26	01:06:04	11.5
2018-10-26	05:48:37	5.5
2018-10-26	12:41:14	8.5
2018-10-26	16:07:10	8.5
2018-10-30	03:00:00	13.0
2018-10-30	08:32:26	17.5
2018-11-01	03:44:49	7.0
2018-11-04	03:12:46	3.0
2018-11-05	06:46:13	5.0
2018-11-11	23:38:35	5.0
2018-11-12	06:50:29	13.0
2018-11-15	09:02:06	8.5
2018-11-15	09:09:27	8.5
2018-11-19	13:05:56	11.0
2018-12-25	01:41:28	8.5
2019-03-17	11:49:40	7.0
2019-05-13	16:57:17	8.5

Table S6. Table summarising the contribution of the various seismic and/or aseismic processes to the overall plate-convergence strain budget. See text for discussion.

Process captured	Slip rate (mm/yr)	% of total convergence rate (26 mm/yr)
Interseismic velocity between Zakynthos/western Peloponnese	21.4	-
Microseismicity	1.3	5
SSEs	2.1	8
Strain released due to seismic/aseismic deformation	3.4	13
Strain stored elastically in the crust	**18**	**69**

Movie S1. Evolution in map-view and cross section (along the transect A-B) of the monthly seismic moment distribution, and equivalent Mw, within the study area. Grey contours in map view and cross section mark the top of the plate-interface (Halpaap et al., 2019). Highlighted with blue contours mark the map-view extent of the transient signal. Inset: timeline indicating the two transient signals (blue rectangles) in 2014 and 2018. See text in the main article for details.

Movie S2. Green arrows and ellipses indicate the daily displacements and respective errors of the GNSS stations. Magenta arrows indicate the daily displacements and respective errors predicted by fluid loading. Scale is shown with the black arrow at the bottom of the plot. Velocities and errors have been estimated from the GNSS and fluid loading displacement time series by using the GrAtSiD algorithm (Bedford and Bevis, 2018) that models trajectories. Displacements shown in this animation are taken from the averaged trajectory model minus the background seasonal oscillation (Fourier terms). Earthquakes from the ZES are plotted as red circles with radius corresponding to the scale (bottom left).

Movie S3. Evolution of the daily velocities of the transient GPS signal with respect to the long-term velocity of each station.

References for the Supplementary Information

Aki, K., 1966. Generation and Propagation of G Waves from the Niigata Earthquake of June 16, 1964.: Part 2. Estimation of earthquake moment, released energy, and stress-strain drop from the G wave spectrum. *Bull.Earthquake Res.Inst., University of Tokyo*, *44*, 73-88.

Albuquerque Seismological Laboratory (ASL)/USGS, 1988. Global Seismograph Network - IRIS/USGS. International Federation of Digital Seismograph Networks. Dataset/Seismic Network. 10.7914/SN/IU

AUTH (Aristotle University of Thessaloniki), 1981. Aristotle University of Thessaloniki Seismological Network. International Federation of Digital Seismograph Networks. 10.7914/SN/HT, https://doi.org/10.7914/SN/HT.

Bedford, J., Bevis, M., 2018. Greedy automatic signal decomposition and its application to daily GPS time series, *J. Geophys. Res.* 123, B014765, 6992–7003.

Cesca, S., Heimann, S., Stammler, K., Dahm, T., 2010. Automated procedure for point and kinematic source inversion at regional distances. *J. Geophys. Res,* 115, doi:10.1029/2009JB006450

Cesca, S., Rohr, A., Dahm, T. 2013. Discrimination of induced seismicity by full moment tensor inversion and decomposition. *J. Seismol.* 17, 1, 147-163, doi:10.1007/s10950-012-9305-8

Cesca, S., 2020. Seiscloud, a tool for density-based seismicity clustering and visualization. *J Seismol*. https://doi.org/10.1007/s10950-020-09921-8

GEOFON Data Centre, 1993. *GEOFON Seismic Network*. Deutsches GeoForschungsZentrum GFZ. https://doi.org/10.14470/TR560404

Grigoli, F., Cesca, S., Rinaldi, A. P., Manconi, A., Lopez Comino, J. A., Clinton, J. F., Westaway, R., Cauzzi, C., Dahm, T., Wiemer, S., 2018. The November 2017 Mw 5.5 Pohang earthquake: A possible case of induced seismicity in South Korea, *Science* 360, 6392, 1003-1006, doi:10.1126/science.aat2010.

Haddad, A., Ganas, A., Kassaras, I., Lupi, M., 2020. Seismicity and geodynamics of western Peloponnese and central Ionian Islands: insights from a local seismic deployment, *Tectonophysics*, https://doi.org/10.1016/j.tecto.2020.228353.

Halpaap, F., Rondenay, S., Perrin, A., Goes, S., Ottemöller, L., Austrheim, H.O., Shaw, R., Eeken, T., 2019. Earthquakes track subduction fluids from slab source to mantle wedge sink. *Sci. Adv.* 5, doi: 10.1126/sciadv.aav7369.

Hanks, T.C., Kanamori, H., 1979. A moment magnitude scale. *J. Geophys. Res.* 84, 2348-2350.

Heimann, S., Isken, M., Kühn, D., Sudhaus, H., Steinberg, A., Vasyura-Bathke, H., Daout, S., Cesca, S., Dahm, T., 2018. Grond - A probabilistic earthquake source inversion framework. V. 1.0. GFZ Data Services. https://doi.org/10.5880/GFZ.2.1.2018.003

INGV Seismological Data Centre, 2006. *Rete Sismica Nazionale (RSN)*. Istituto Nazionale di Geofisica e Vulcanologia (INGV), Italy. https://doi.org/10.13127/SD/X0FXNH7QFY

INGV (Istituto Nazionale di Geofisica e Vulcanologia), 2009. Emersito Seismic Network for Site Effect Studies in L'Aquila town (Central Italy). International Federation of Digital Seismograph Networks. Dataset/Seismic Network. 10.7914/SN/4A_2009

Institute of Geosciences, Energy, Water and Environment, 2002. Albanian Seismological Network. International Federation of Digital Seismograph Networks. Dataset/Seismic Network. 10.7914/SN/AC

Institut De Physique Du Globe De Paris (IPGP), & Ecole Et Observatoire Des Sciences De La Terre De Strasbourg (EOST), 1982. *GEOSCOPE, French Global Network of broad band seismic stations*. Institut de Physique du Globe de Paris (IPGP). https://doi.org/10.18715/GEOSCOPE.G

Kassaras, I., Kapetanidis, V., Karakonstantis, A., 2016. On the spatial distribution of seismicity and the 3D tectonic stress field in western Greece. *Phys. Chem. Earth.* 95, 50-72.

Lomax, A., Michelini, A., Curtis, A., 2009. Earthquake Location, Direct, Global-Search Methods, in: Meyers, R.A. (Ed.), Encyclopedia of Complexity and Systems Science. Springer New York, New York, NY, pp. 2449–2473.

Lomax, A., Virieux, J., Volant, P., Berge-Thierry, C., 2000. Probabilistic earthquake location in 3D and layered models, in: Thurber, C.H., Rabinowitz, N. (Eds.), Advances in Seismic Event Location. Springer, Dordrecht, Kluwer, Amsterdam, pp. 101–134.

MedNet Project Partner Institutions, 1990. *Mediterranean Very Broadband Seismographic Network (MedNet)*. Istituto Nazionale di Geofisica e Vulcanologia (INGV). https://doi.org/10.13127/SD/FBBBTDTD6Q

NOA (National Observatory of Athens), Institute of Geodynamics, Athens, 1997. National Observatory of Athens Seismic Network. International Federation of Digital Seismograph Networks. Dataset/Seismic Network. 10.7914/SN/HL, https://doi.org/10.7914/SN/HL.

Negi, S. S., Paul, A., Cesca, S., Kamal, Kriegerowski, M., Mahesh, P., Gupta, S., 2017. Crustal velocity structure and earthquake processes of Garhwal-Kumaun Himalaya: Constraints from regional waveform inversion and array beam modeling, *Tectonophysics* 712, 45-63, doi:10.1016/j.tecto.2017.05.007

NOA (National Observatory of Athens), Institute of Geodynamics, Athens, 1997. National Observatory of Athens Seismic Network. International Federation of Digital Seismograph Networks. Dataset/Seismic Network, https://doi.org/10.7914/SN/HL.

Okada, Y., 1985. Surface deformation due shear and tensile faults in a half-space. *Bull. Seismol. Soc. Am.* 75, 1135–1154.

Pearce, D., Rondenay, S., Sachpazi, M., Charalampakis, M., Royden, L.H., 2012. Seismic investigation of the transition from continental to oceanic subduction along the western Hellenic subduction Zone. *J. Geophys. Res.* 117, 1–18. https://doi.org/10.1029/2011JB009023

Pérouse, E., Sébrier, M., Braucher, R., Chamot-Rooke, N., Bourlès, D., Briole, P., Sorel, D., Dimitrov, D., Arsenikos, S., 2017. Transition from collision to subduction in Western Greece: the Katouna–Stamna active fault system and regional kinematics. *Intern. J. Earth Sci.* 106, 967–989, doi:10.1007/s00531-016-1345-9.

Scripps Institution of Oceanography, 1986. Global Seismograph Network - IRIS/IDA. International Federation of Digital Seismograph Networks. Dataset/Seismic Network. 10.7914/SN/II

Sokos, E., 2015. Lefkada temporary network. International Federation of Digital Seismograph Networks. Dataset/Seismic Network. 10.7914/SN/X5_2015

Sokos, E., Gallovič, F., Evangelidis, C. P., Serpetsidaki, A., Plicka, V., Kostelecký, J., Zahradník, J., 2020. The2018Mw6.8 Zakynthos, Greece,Earthquake: Dominant Strike-Slip Faultingnear Subducting Slab, *Seismol. Res. Lett.*, doi:10.1785/0220190169

UA (University of Athens), 2008. Hellenic Seismological Network, University of Athens, Seismological Laboratory. International Federation of Digital Seismograph Networks. Dataset/Seismic Network. 10.7914/SN/HA

UP (University of Patras), 2000. University of Patras, Seismological Laboratory. International Federation of Digital Seismograph Networks. Dataset/Seismic Network. 10.7914/SN/HP

Utsu T., 1965. A method for determining the value of b in a formula 329 log n = a - bM showing the magnitude-frequency relation for 330 earthquakes. *Geophys. Bull., Hokkaido Univ.* 13, 99–103.

Wiemer, S., Wyss, M., 2000. Minimum magnitude of completeness in earthquake catalogs: Examples from Alaska, the Western United States, and Japan. *Bull. Seismol. Soc. Am.* 90, 859–869.